Draft version January 28, 2014
Preprint typeset using LaTeX style emulateapj v. 5/2/11

arXiv:1401.1210v2 [astro-ph.EP] 26 Jan 2014

THE HUNT FOR EXOMOONS WITH KEPLER (HEK): IV. A SEARCH FOR MOONS AROUND EIGHT M-DWARFS †

D. M. Kipping[1,2], D. Nesvorný[3], L. A. Buchhave[4,5], J. Hartman[6], G. Á. Bakos[6,7,8], A. R. Schmitt[9]

Draft version January 28, 2014

ABSTRACT

With their smaller radii and high cosmic abundance, transiting planets around cool stars hold a unique appeal. As part of our on-going project to measure the occurrence rate of extrasolar moons, we here present results from a survey focussing on eight *Kepler* planetary candidates associated with M-dwarfs. Using photodynamical modeling and Bayesian multimodal nested sampling, we find no compelling evidence for an exomoon in these eight systems. Upper limits on the presence of such bodies probe down to masses of $\sim 0.4\,M_\oplus$ in the best case. For KOI-314, we are able to confirm the planetary nature of two out of the three known transiting candidates using transit timing variations. Of particular interest is KOI-314c, which is found to have a mass of $1.0^{+0.4}_{-0.3}\,M_\oplus$, making it the lowest mass transiting planet discovered to date. With a radius of $1.61^{+0.16}_{-0.15}\,R_\oplus$, this Earth-mass world is likely enveloped by a significant gaseous envelope comprising $\geq 17^{+12}_{-13}\%$ of the planet by radius. We also find evidence to support the planetary nature of KOI-784 via transit timing, but we advocate further observations to verify the signals. In both systems, we infer that the inner planet has a higher density than the outer world, which may be indicative of photo-evaporation. These results highlight both the ability of *Kepler* to search for sub-Earth mass moons and the exciting ancillary science which often results from such efforts.

Subject headings: techniques: photometric — planetary systems — planets and satellites: detection — stars: individual (KIC-8845205, KIC-7603200, KIC-12066335, KIC-6497146, KIC-6425957, KIC-10027323, KIC-3966801, KIC-11187837; KOI-463, KOI-314, KOI-784, KOI-3284, KOI-663, KOI-1596, KOI-494, KOI-252)

1. INTRODUCTION

In recent years, there has been a concerted effort to determine the occurrence rate of small planets around main-sequence stars across a broad range of spectral types and orbital period using various observational techniques and strategies (e.g. Howard et al. 2010; Mayor et al. 2011; Bonfils et al. 2013; Fressin et al. 2013; Dressing & Charbonneau 2013; Dong & Zhu 2013; Petigura et al. 2013). The emerging consensus from these studies is that small planets are indeed common with occurrence rates ranging from 5%-90% for different size and periods ranges. What remains wholly unclear is the occurrence rate of "large" ($\gtrsim 0.1\,M_\oplus$) moons around viable planet hosts. Like mini-Neptunes and super-Earths, there are no known examples of such objects in the Solar System but their prevalence would provide deep insights into the formation and evolution of planetary systems, as well as providing a potentially frequent seat for life in the cosmos (Williams et al. 1997; Heller 2012; Heller et al. 2013; Forgan & Kipping 2013).

Determining the occurrence rate of large moons constitutes the primary objective the "Hunt for Exomoons with Kepler" (HEK) project, which seeks evidence of transiting satellites in the *Kepler* data (Kipping et al. 2012). By establishing the occurrence rate as our primary objective, the strategy of our survey requires careful consideration of upper limits and prior inputs and is therefore substantially more challenging than a simple "fishing-trip" style survey. For these reasons, HEK conducts the survey in a rigorous Bayesian framework, which comes at the acceptable cost of higher computational demands.

In previous works, we have surveyed eight planetary candidates around G and K dwarfs for evidence of exomoons, with no compelling evidence for such an object identified thus far (Kipping et al. 2013a,b). Despite null detections, Earth-mass and sub-Earth-mass moons are excluded in many cases (Kipping et al. 2013a). Although there have been no transiting exomoon candidates published at this time, recently Bennett et al. (2013) reported a candidate free floating planet-moon pair via microlensing for MOA-2011-BLG-262. Unfortunately, this object cannot be distinguished from a high velocity planetary system in the Galactic bulge (Bennett et al. 2013), nor is there much prospect of obtaining a repeat measurement to confirm the signal. At this time, the sample of planets for which statistically robust limits has been determined is too small to broach the question of occurrence rates. The purpose of this work is to extend the

[1] Harvard-Smithsonian Center for Astrophysics, Cambridge, MA 02138, USA; email: dkipping@cfa.harvard.edu
[2] NASA Carl Sagan Fellow
[3] Dept. of Space Studies, Southwest Research Institute, 1050 Walnut St., Suite 300, Boulder, CO 80302, USA
[4] Niels Bohr Institute, University of Copenhagen, DK-2100, Copenhagen, Denmark
[5] Centre for Star and Planet Formation, Natural History Museum of Denmark, University of Copenhagen, DK-1350, Copenhagen, Denmark
[6] Dept. of Astrophysical Sciences, Princeton University, Princeton, NJ 05844, USA
[7] Alfred P. Sloan Fellow
[8] Packard Fellow
[9] Citizen Science
† Based on archival data of the *Kepler* telescope.

sample of planetary candidates which have been systematically and thoroughly examined for evidence of exomoons.

For our second systematic survey, we focus on planetary candidates orbiting M-dwarfs ($T_{\rm eff} < 4000\,{\rm K}$) in the *Kepler* sample. Although considerably rarer than FGK hosts in a magnitude limited survey like *Kepler* (Dressing & Charbonneau 2013), M-dwarfs offer several major advantages for seeking exomoons. The most crucial advantage is that since the stars are typically two to three times smaller than a Sun-like host, an Earth-sized moon produces a four to nine times greater transit depth. This advantage is somewhat tempered by the lower intrinsic luminosities of the targets, leading to fainter apparent magnitudes (median *Kepler* magnitude of our sample is 14.8) and thus higher photometric noise. However, at such faint magnitudes, *Kepler's* noise budget is photon-dominated and thus the chance of instrumental and time-correlated noise inducing spurious photometric signals masquerading as moons is considerably attenuated. Finally, we note that for all things being equal except the spectral type of a host star, a planet's Hill radius for stable moon orbits is modestly larger (by 25-45%) in M-dwarf systems. The great unknown we cannot factor into our choice of spectral types is whether the underlying occurrence rate of large moons is fundamentally distinct for M-dwarfs than other spectral types, since no confirmed detections of exomoons exist at this time.

2. METHODS

2.1. *Target Selection (TS)*

From the thousands KOIs (Kepler Objects of Interest) known at this time, we aim to trim the sample down to just eight objects for our survey. This is necessary since each object requires decades worth of computational time to process (Kipping et al. 2013b). The first cut we make was defined earlier in the introduction, where we only consider host stars for which $T_{\rm eff} < 4000\,{\rm K}$. Reliable stellar parameters are challenging to determine for these cool faint stars but recent near-infrared spectroscopy campaigns by Muirhead et al. (2012) and Muirhead et al. (2014) provide arguably the most accurate estimates for the cool KOIs. We therefore limit our sample to only M-dwarfs included in these two catalogs, which contains 203 KOIs spread over 134 host stars.

In this work, Target Selection (TS) is conducted using the Target Selection Automatic (TSA) algorithm described in Kipping et al. (2012) and updated in Kipping et al. (2013a). From the 203 KOIs in the Muirhead et al. (2012) and Muirhead et al. (2014) catalogs, we only further consider KOIs which satisfy the following criteria: i) dynamically capable of maintaining a retrograde Earth-mass moon for 5 Gyr following the calculation method outlined in Kipping et al. (2012) (which uses the expressions of Barnes & O'Brien 2002 and Domingos et al. 2006), ii) an Earth-sized transit with the same duration as that of the KOI would be detectable to $\Sigma{\rm SNR} > 7.1$ when all transit epochs are used and iii) an Earth-sized transit with the same duration as that of the KOI would be detectable to ${\rm SNR}_i > 1$ for a single transit epoch. These three constraints are the same as those in Kipping et al. (2012) except that we slightly modify the SNR equation to account for transit duration more appropriately using

$$ {\rm SNR}_i = \frac{(R_\oplus/R_\star)^2}{{\rm CDPP}_6}\sqrt{\frac{T_{14}}{6\,{\rm hours}}}, \quad (1) $$

$$ \Sigma{\rm SNR} = {\rm SNR}_i\sqrt{N_{\rm transits}}, \quad (2) $$

where ${\rm CDPP}_6$ is the Combined Differential Photometric Precision over 6 hours (Christiansen et al. 2012), T_{14} is the first-to-fourth contact duration, $N_{\rm transits}$ is the number of usable transits in the time series, $R_\oplus$ is one Earth-radius and $R_\star$ is the stellar radius. These filters leave us with 27 KOIs from which we have selected eight objects to study in this work. The eight planetary candidates are listed along with some basic parameters in Table 1. Additionally, we list the employed stellar parameters of each host star in Table 2.

We noted that KOI-314, being an unusually bright *Kepler* M-dwarf at 12.9 apparent magnitude, has considerably more follow-up available than the other seven targets. Specifically, Pineda et al. (2013) have derived stellar parameters for this object by stacking high-resolution spectra taken from Keck/HIRES and comparing to empirically derived templates of well-characterzied M-dwarfs. We therefore use the Pineda et al. (2013) stellar parameters rather than those of Muirhead et al. (2014) for this unique case. Pineda et al. (2013) do not provide the effective temperature, however, and so we defer to the measurement of Mann et al. (2013) for this parameter.

2.2. *Detrending with* `CoFiAM`

In order to search for the very small expected amplitudes of exomoon signals and accurately model the planetary transits, it is necessary to remove the flux variations due to both instrumental effects and several astrophysical effects. In what follows, we use the Simple Aperture Photometry (SAP) for quarters 1-15 and perform our own detrending rather than relying on the Presearch Data Conditioning (PDC) data. Short-cadence (SC) data is used preferentially to long-cadence (LC) data wherever available. Short-term variations such as flaring, pointing tweaks and safe-mode recoveries (charge trapping) are removed manually by simple clipping techniques. Long-term variations, such as focus drift and rotational modulations, are detrended using the Cosine Filtering with Autocorrelation Minimization (`CoFiAM`) algorithm. `CoFiAM` was specifically developed to aid in searching for exomoons and we direct the reader to our previous papers Kipping et al. (2012, 2013a) for a detailed description.

To summarize the key features of `CoFiAM`, it is essentially a Fourier-based method which removes periodicities occurring at timescales greater than the known transit duration. This process ensures that the transit profile is not distorted and if we assume that a putative exomoon does not display a transit longer than the known KOI, then the moon's signal is also guaranteed to be protected. `CoFiAM` does not directly attempt to remove high frequency noise since this process could also easily end up removing the very small moon signals we seek. However, `CoFiAM` is able to attempt dozens of different harmonics and evaluate the autocorrelation at a preselected timescale (we use 30 minutes) and then select the harmonic order which minimizes this autocorrelation, as

TABLE 1
General properties of the planet candidates studied in this work and used as inputs for our TSA algorithm. SNR (Signal-to-Noise Ratio) is defined in Equation 2. Planetary radii were taken from the Muirhead et al. (2012), except for KOI-1596.02 for which we use Dressing & Charbonneau (2013) radius.

KOI	P_P [days]	R_P [$R_\oplus$]	SNR_i	SNR	Multiplicity	$T_{\rm eq}$ [K]	K_P
KOI-463.01	18.5	1.50	3.27	30.37	1	268	14.7
KOI-314.02	23.0	1.68	4.07	33.74	3	431	12.9
KOI-784.01	19.3	1.67	1.20	10.86	2	395	15.4
KOI-3284.01	35.2	0.91	2.24	15.02	1	286	14.5
KOI-663.02	20.3	1.58	3.52	31.16	2	534	13.5
KOI-1596.02	105.4	2.35	1.87	7.27	2	308	15.2
KOI-494.01	25.7	1.65	2.23	17.50	1	405	14.9
KOI-252.01	17.6	2.36	1.43	13.59	1	472	15.6

TABLE 2
General properties of the planet candidate host stars studied in this work. Last column provides the reference from which we lift the stellar parameters. † implies effective temperature comes from Mann et al. (2013) instead of the quoted reference.

KOI	$T_{\rm eff}$ [K]	$\log g$	M_* [$M_\odot$]	R_* [$R_\odot$]	Sp. Type	Reference
KOI-463	3389^{+57}_{-41}	$4.96^{+0.14}_{-0.13}$	0.32 ± 0.05	0.31 ± 0.04	M3V	Muirhead et al. (2014)
KOI-314	3871^{+58}_{-58} †	$4.73^{+0.09}_{-0.09}$	0.57 ± 0.05	0.54 ± 0.05	M1V	Pineda et al. (2013)
KOI-784	3767^{+135}_{-51}	$4.78^{+0.13}_{-0.12}$	0.51 ± 0.06	0.48 ± 0.06	M1V	Muirhead et al. (2012)
KOI-3284	3748^{+50}_{-100}	$4.75^{+0.08}_{-0.07}$	0.55 ± 0.04	0.52 ± 0.04	M1V	Muirhead et al. (2014)
KOI-663	3834^{+50}_{-57}	$4.78^{+0.13}_{-0.12}$	0.51 ± 0.06	0.48 ± 0.06	M1V	Muirhead et al. (2012)
KOI-1596	3880^{+143}_{-103}	$4.77^{+0.14}_{-0.14}$	0.51 ± 0.07	0.49 ± 0.07	M0V	Muirhead et al. (2012)
KOI-494	3789^{+219}_{-159}	$4.78^{+0.22}_{-0.20}$	0.50 ± 0.10	0.48 ± 0.10	M1V	Muirhead et al. (2012)
KOI-252	3745^{+53}_{-71}	$4.76^{+0.06}_{-0.06}$	0.54 ± 0.03	0.51 ± 0.03	M1V	Muirhead et al. (2014)

quantified using the Durbin-Watson statistic. This "Autocorrelation Minimization" component of `CoFiAM` provides optimized data for subsequent analysis. In contrast to the initial sample studied in Kipping et al. (2013a), we found that none of the eight detrended KOI light curves retained significant ($> 3\,\sigma$) autocorrelation after `CoFiAM`, which is consistent with a photon-noise dominated sample, which one might expect for these generally fainter targets.

2.3. *Light Curve Fits*

The transit light curves for a planet-with-moon scenario (model $\mathcal{S}$) are modeled using the analytic photodynamical algorithm `LUNA` (Kipping 2011a), as with previous HEK papers. Photodynamical modeling accounts for not only the transits of the planet and the moon but also the transit timing and duration variations (TTVs and TDVs) expected (Kipping 2009a,b) in a dynamic framework. These fits always assume just a single moon and thus our search is implicitly limited to such cases. For comparison, we consider a simple planet-only model (model $\mathcal{P}$) as well, for which we employ the standard Mandel & Agol (2002) routine. Finally, we perform a planet fit on each individual transit to derive TTVs and TDVs (model $\mathcal{I}$), which is useful in comparing our moon model against perturbing planet models later on.

Light curve fits are performed in a Bayesian framework with the goal of both deriving parameter posteriors and computing the Bayesian evidence ($\mathcal{Z}$) for each model. The moon fits are particularly challenging requiring 14 free parameters exhibiting a large number of modes and complex inter-parameter correlations. To this end, we employ the multimodal nested sampling algorithm MultiNest (Feroz et al. 2008, 2009) as with previous HEK papers. For all fits, we use 4000 live points with a target efficiency of 0.1 and use the same parameter sets and priors described in Kipping et al. (2013a), giving us 7 free parameters for model $\mathcal{P}$ and 14 for $\mathcal{S}$. The only change from the Kipping et al. (2013a) priors, is that we fit the quadratic limb darkening coefficients using the q_1-q_2 parameter set suggested in Kipping (2013a), which provides more efficient parameter exploration. Contamination factors for each quarter are accounted for using the method devised in Kipping & Tinetti (2010) and long-cadence data is resampled using $N_{\rm resam} = 30$ following the technique devised in Kipping (2010).

In Kipping et al. (2013a), we described four basic detection criteria (B1-B4) to test whether an exomoon fit can be further considered as a candidate or not. The criteria essentially demand that the moon signal is both significant and physically reasonable:

B1 Improved evidence of the planet-with-moon fits at $\geq 4\,\sigma$ confidence.

B2 Planet-with-moon evidences indicate a preference for a) a non-zero radius moon b) a non-zero mass moon.

B3 Parameter posteriors are physical, in particular ρ_P.

B4 a) Mass and b) radius of the moon converge away from zero.

One slight difference to Kipping et al. (2013a) is that we have split some of the basic detection criteria into subcriteria. This will be useful later since it is often easier to evaluate just a subset of the sub-criteria and a failure to pass one of these allows us to quickly reject the object as an exomoon candidate. Note that in practice we reject any trials for which the density of the planet is excessively

low and this causes the radius of the moon to be non-zero and so criterion B4b is always satisfied by virtue of the priors used in our model. B4a is defined as being satisfied if there is a less than a 5% false-alarm-probability of the satellite-to-planet mass ratio (M_S/M_P) being zero using the Lucy & Sweeney (1971) test.

Another change we implement follows the strategy used recently for Kepler-22b (Kipping et al. 2013b), where we allow `LUNA` to model negative-radius moons (which we treat as inverted transits) during model $\mathcal{S}$. By doing so, it is no longer necessary to run a separate moon fit to test B2a, where we would have previously locked the radius to zero (although this fit is sometimes still a useful tool). This trick essentially saves computation time yet retains our ability to test sub-criterion B2a. We define that sub-criterion B2a is unsatisfied if the 38.15% quantile (lower $1\,\sigma$ quantile) of the derived satellite-to-planet radius ratio (R_S/R_P) is negative.

Although we use precisely the same definition for B1 as that of previous papers, we reiterate here that B1 is computed by evaluating if the Bayesian evidences between models $\mathcal{P}$ and $\mathcal{S}$ indicates a $\geq 4\,\sigma$ preference for the latter.

If all of the basic detection criteria are satisfied, we also have three follow-up criteria described in Kipping et al. (2013a) to further vet candidates. The concept here is to only fit 75% of the available data in the original transit fits and thus deliberately exclude 25% of time series, which serves as "follow-up" data.

F1 All four basic criteria are still satisfied when new data is included.

F2 The predictive power of the moon model is superior to that of a planet-only model.

F3 A consistent and statistically enhanced signal is recovered with the inclusion of more data.

The most powerful of these criteria is F2 and this test is performed for all KOIs studied in this work. In Kipping et al. (2013a), the 75% original data was considered to be quarters 1-9 and the follow-up data was quarter 10-12. In this framework, F2 tests the extrapolated best moon model fit. One significant change in this work is that we now choose the 25% follow-up data to lie somewhere around the middle of our total available time series. This means that F2 now tests an *interpolation* of the model rather than an *extrapolation*. An advantage of doing this is that parameters such as the orbital period of the planet are best constrained by maximizing the baseline of available data and so this new approach allows for improved parameter estimates.

3. RESULTS

3.1. *Overview*

In this work, all eight KOIs can be placed into one of three categories: i) null detections (§3.2), ii) spurious photometric detections (§3.3) and iii) spurious dynamical detections (§3.4). Each category is defined in the relevant subsection but it should be clear from their naming that we find no confirmed or candidate exomoons in this sample. For each KOI system studied, the TTVs and TDVs of all planetary candidates can be seen in Figures 1-8. Parameter estimates from the marginalized posteriors of the favored light curve model are provided for all KOIs in Table 3, except KOI-314 and KOI-784 which are available later in Table 6.

3.2. *Null Detections*

The first category of objects we discuss in this section are the null detections. We define these objects to be ones for which the mode of the derived satellite-to-planet mass ratio (M_S/M_P) posterior distribution is at, or close to, zero plus other detection criteria are also failed. Note that this is distinct from requiring that the objects fail criterion B4a, although any object in this category will indeed fail B4a too. We find five objects in this category: KOI-663.02, KOI-1596.02, KOI-494.01, KOI-463.01 and KOI-3284.01. Null detections, such as these, allow for a simple calculation of the upper limit on the ratio (M_S/M_P) by posterior marginalization. These upper limits range from 0.29 to 0.92 (95% confidence upper limits) and are available in Table 3.

As well as failing criteria B4a, all of these objects fail at least one other detection criteria, as listed in Table 4. For several cases, a periodogram search of the TTVs and TDVs for these objects appears to indicate possible perturbations, as shown in Figures 1-5. We have listed the most significant peaks from a periodogram search in Table 5.

KOI-463.01 and KOI-3284.01 are two single KOI systems which show $> 4\,\sigma$ significant TTVs (from an F-test). This may therefore be evidence for additional planets although we consider the signal-to-noise of the available data insufficient to reliably deduce a unique unseen perturber solution. We consider the TTVs/TDVs of the only other single KOI classed as an exomoon null-detection, KOI-494.01, to be insignificant.

Two out of the five null detection cases reside in multi-transiting planet systems where interactions may be a-priori expected. However, the period ratios between KOI-663.02/KOI-663.01 and KOI-1596.02/KOI-1596.01 are 7.4 and 17.8 respectively i.e. too far to expect significant interactions. This point is reinforced empirically by noting that the periodograms show no strong overlapping peaks and no significant ($\geq 4\,\sigma$) power. We are therefore unable to confirm these two multi-planetary systems using TTVs.

3.3. *Spurious Photometric Detections*

A spurious photometric detection is one where we hypothesize that a residual amount of time-correlated noise drives a non-zero satellite radius solution, which then itself drives a non-zero satellite mass solution due to the fact we enforce only physically reasonable satellite densities in the fits. We identify such cases by the fact that: i) the posterior distribution for (M_S/M_P) does not peak at zero (and thus it is not a "null" detection), ii) other detection criteria are failed (suggesting some kind of spurious detection) and iii) performing a fit where the moon's radius is fixed to zero (model $\mathcal{S}_{R0}$) yields an (M_S/M_P) posterior which peaks at zero, as expected for a null detection. This final point indicates that when we switch off the moon's radius, the planet no longer seems to be perturbed and thus the moon's radius was likely a result of the regression fitting out non-astrophysical artifacts

TABLE 3
Final parameter estimates from the favored light curve model for KOIs studied in our sample, except KOI-314 and KOI-784 which are provided in Table 6. In all cases, the favored model is a simple planet-only model.

KOI	463.01	3284.01	663.02	1596.02	494.01	252.01
P	$18.477637^{+0.000014}_{-0.000014}$	$35.23266^{+0.00027}_{-0.00026}$	$20.306531^{+0.000023}_{-0.000022}$	$105.35794^{+0.00060}_{-0.00064}$	$25.695907^{+0.000070}_{-0.000070}$	$18.604627^{+0.00022}_{-0.000022}$
τ [BKJD$_{\rm UTC}$] .	$758.07461^{+0.00033}_{-0.00033}$	$769.5611^{+0.0036}_{-0.0034}$	$781.85484^{+0.00049}_{-0.00049}$	$665.4733^{+0.0023}_{-0.0023}$	$779.7936^{+0.0012}_{-0.0012}$	$874.68224^{+0.00055}_{-0.00052}$
$(R_P/R_\star)$	$0.0475^{+0.0011}_{-0.0010}$	$0.01837^{+0.011}_{-0.010}$	$0.02431^{+0.00105}_{-0.00055}$	$0.0355^{+0.0020}_{-0.0018}$	$0.03246^{+0.0107}_{-0.0095}$	$0.0457^{+0.0035}_{-0.0022}$
$\rho_{\star,\rm obs}$ [g cm^{-3}]	$27.0^{+3.8}_{-8.5}$	$3.41^{+0.98}_{-1.45}$	$7.2^{+1.1}_{-2.4}$	$15.5^{+3.7}_{-6.6}$	$3.64^{+0.60}_{-1.35}$	$2.1^{+1.5}_{-1.2}$
b	$0.29^{+0.25}_{-0.20}$	$0.30^{+0.32}_{-0.21}$	$0.31^{+0.26}_{-0.21}$	$0.31^{+0.31}_{-0.21}$	$0.30^{+0.29}_{-0.21}$	$0.58^{+0.21}_{-0.38}$
q_1	$0.22^{+0.28}_{-0.13}$	$0.43^{+0.36}_{-0.28}$	$0.42^{+0.25}_{-0.14}$	$0.50^{+0.32}_{-0.28}$	$0.27^{+0.33}_{-0.17}$	$0.47^{+0.32}_{-0.20}$
q_2	$0.29^{+0.38}_{-0.21}$	$0.44^{+0.35}_{-0.30}$	$0.62^{+0.25}_{-0.26}$	$0.51^{+0.31}_{-0.31}$	$0.37^{+0.38}_{-0.25}$	$0.27^{+0.36}_{-0.17}$
R_P [$R_\oplus$]	$1.61^{+0.21}_{-0.21}$	$1.04^{+0.11}_{-0.10}$	$1.28^{+0.17}_{-0.16}$	$1.90^{+0.30}_{-0.29}$	$1.70^{+0.36}_{-0.36}$	$2.56^{+0.23}_{-0.20}$
u_1	$0.48^{+0.18}_{-0.20}$	$0.78^{+0.45}_{-0.40}$	$0.99^{+0.13}_{-0.14}$	$0.91^{+0.38}_{-0.38}$	$0.59^{+0.25}_{-0.26}$	$0.74^{+0.17}_{-0.25}$
u_2	$-0.03^{+0.30}_{-0.18}$	$-0.18^{+0.32}_{-0.30}$	$-0.36^{+0.20}_{-0.11}$	$-0.26^{+0.33}_{-0.26}$	$-0.10^{+0.30}_{-0.19}$	$-0.03^{+0.31}_{-0.29}$
$S_{\rm eff}$ [$S_\oplus$]	$0.896^{+0.248}_{-0.098}$	$2.23^{+0.99}_{-0.38}$	$3.12^{+0.96}_{-0.35}$	$0.221^{+0.100}_{-0.041}$	$3.54^{+1.41}_{-0.80}$	$7.7^{+5.4}_{-2.3}$
$(\rho_{\star,\rm obs}/\rho_{\star,\rm true})$	$1.65^{+0.97}_{-0.70}$	$0.59^{+0.27}_{-0.26}$	$1.01^{+0.57}_{-0.42}$	$2.3^{+1.7}_{-1.2}$	$0.51^{+0.51}_{-0.29}$	$0.36^{+0.26}_{-0.19}$
$e_{\rm min}$	$0.18^{+0.14}_{-0.12}$	$0.18^{+0.18}_{-0.13}$	$0.00^{+0.17}_{-0.00}$	$0.00^{+0.17}_{-0.00}$	$0.22^{+0.25}_{-0.22}$	$0.33^{+0.21}_{-0.17}$
(M_S/M_P)	< 0.92	< 0.29	< 0.52	< 0.60	< 0.66	< 0.32

TABLE 4
Detection criteria results for each of the eight KOIs surveyed in this work. Only KOI-314.02 and KOI-784.01 pass the five criteria listed here.

KOI	B1	B2a	B3a	B4a	F2
KOI-463.01	X ($+2.89\,\sigma$)	X (-0.33)	✓ (4.82%)	X (FAP=29.86%)	X ($\Delta\chi^2 = 27.8$ for $N = 1815$)
KOI-314.02	✓ ($+14.3\,\sigma$)	✓ ($+0.28$)	✓ (0.00%)	✓ (FAP=0.066%)	✓ ($\Delta\chi^2 = -925.0$ for $N = 9161$)
KOI-784.01	✓ ($+6.50\,\sigma$)	✓ ($+0.32$)	✓ (0.00%)	✓ (FAP=0.018%)	✓ ($\Delta\chi^2 = -39.0$ for $N = 9431$)
KOI-3284.01	X ($+3.32\,\sigma$)	✓ ($+0.58$)	X (94.2%)	X (FAP=37.28%)	X ($\Delta\chi^2 = 15.8$ for $N = 597$)
KOI-663.02	X ($+0.76\,\sigma$)	X (-0.44)	X (38.8%)	X (FAP=47.61%)	X ($\Delta\chi^2 = 12.8$ for $N = 9676$)
KOI-1596.02	X ($+1.62\,\sigma$)	✓ ($+0.34$)	✓ (2.09%)	X (FAP=34.13%)	✓ ($\Delta\chi^2 = -4.1$ for $N = 322$)
KOI-494.01	X ($+1.23\,\sigma$)	X (-0.46)	X (39.6%)	X (FAP=30.55%)	X ($\Delta\chi^2 = 16.0$ for $N = 836$)
KOI-252.01	X ($+1.82\,\sigma$)	✓ ($+0.52$)	✓ (0.40%)	X (FAP=16.13%)	✓ ($\Delta\chi^2 = -4.9$ for $N = 33048$)

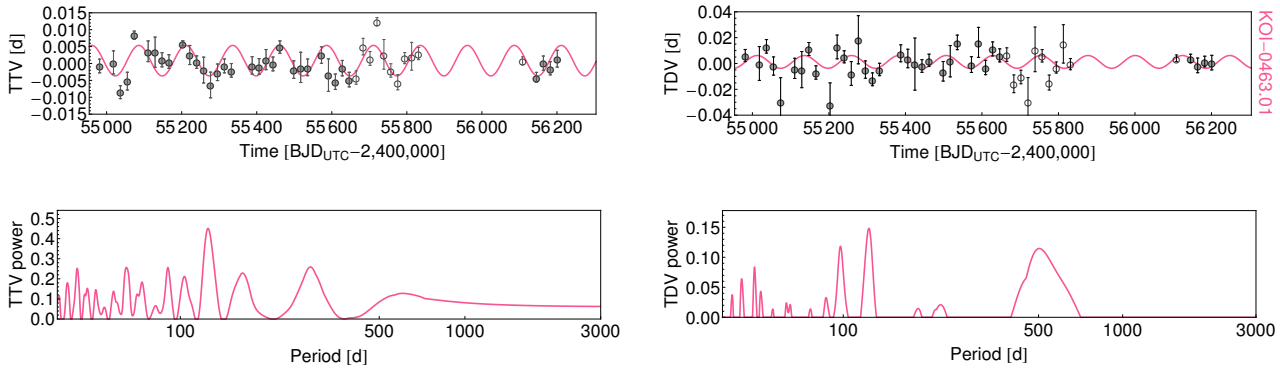

FIG. 1.— *TTVs (left) and TDVs (right) for the planetary candidate of KOI-463. Points used in the photodynamical moon fits are filled circles, whereas those points ignored for subsequent predictive tests are open circles. Bottom panels show the periodograms of the TTVs & TDVs (which use the entire available data set).*

in the light curve. KOI-252.01 is the only object in this survey which we classify in this category.

As seen in Table 4, B1 and B4a are both failed for KOI-252.01. The latter is because the derived (M_S/M_P) peaks away from zero (at around 0.5) and yet is extremely disperse over the entire prior. The former essentially implies that whatever is driving the fit is actually of relatively low significance.

By definition of being a spurious photometric detection, the (M_S/M_P) posterior has a mode at zero when we enforce $(R_S/R_P) = 0$ in the 13-dimensional model $\mathcal{S}_{R0}$. The results from this model are now consistent with a null detection and thus we may derive upper limits on (M_S/M_P) as usual (this is similar to the procedure used for KOI-303.01 in Kipping et al. 2013a). For KOI-252.01 then, we derive that $(M_S/M_P) < 0.33$ to 95% confidence.

3.4. *Spurious Dynamical Detections*

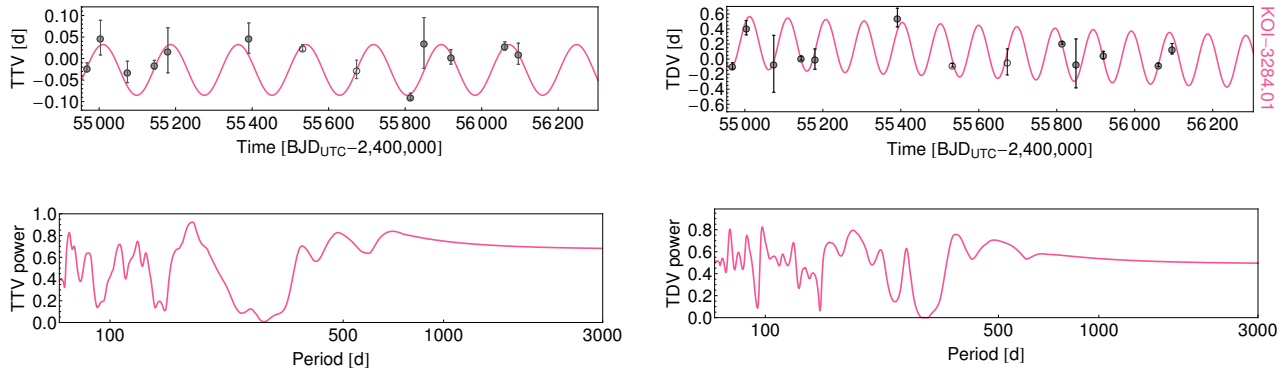

FIG. 2.— *TTVs (left) and TDVs (right) for the planetary candidate of KOI-3284. Points used in the photodynamical moon fits are filled circles, whereas those points ignored for subsequent predictive tests are open circles. Bottom panels show the periodograms of the TTVs & TDVs (which use the entire available data set).*

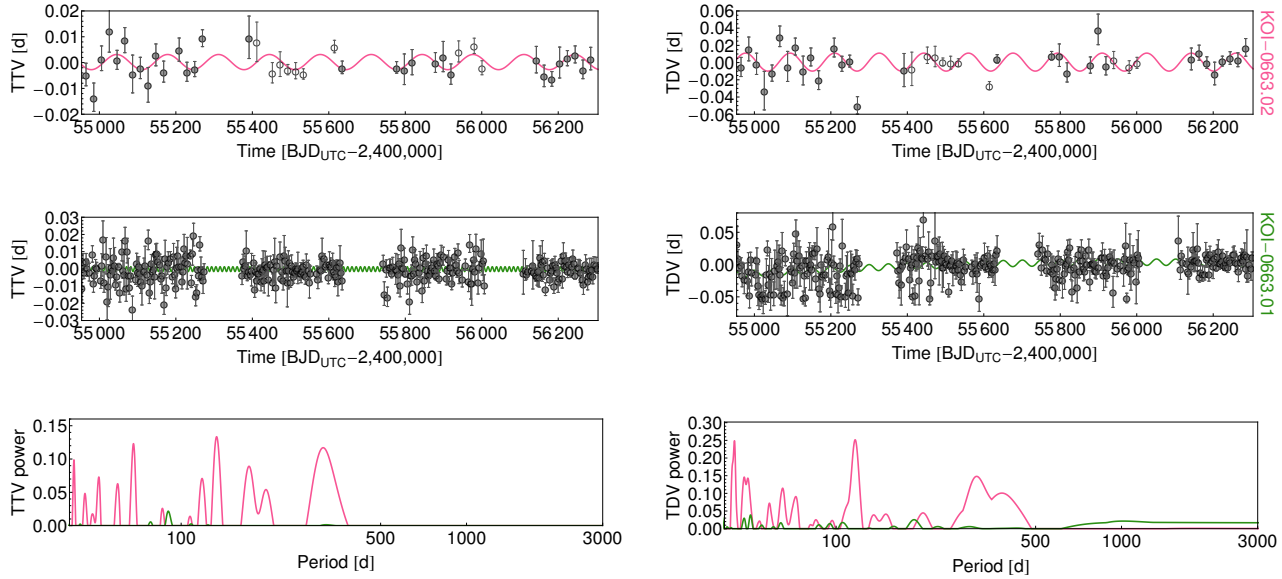

FIG. 3.— *TTVs (left) and TDVs (right) for the planetary candidates of KOI-663. Each row shows the observations (circles) with the best-fit sinusoid from a periodogram using the same coloring as that for which the name of the planet is highlighted in on the RHS. For KOI-663.02, points used in the photodynamical moon fits are filled circles, whereas those points ignored for subsequent predictive tests are open circles. Bottom panels show the periodograms of the TTVs & TDVs (which use the entire available data set), with vertical grid lines marking the locations where one might expect power from planet-planet interactions.*

TABLE 5
Summary of the highest power peaks found in the periodograms of the TTVs and TDVs of the planetary candidates analyzed in this work.

KOI	TTV Period [d]	TTV Amp. [mins]	TTV Signif.	TDV Period [d]	TDV Amp. [mins]	TDV Signif.
KOI-463.01	125.1	6.5	4.8 σ	123.6	7.1	2.3 σ
KOI-314.02	112.9	21.7	9.3 σ	307.3	6.9	3.9 σ
KOI-314.01	913.8	2.5	3.8 σ	38.7	3.1	2.4 σ
KOI-314.03	434.0	16.4	3.2 σ	-	-	-
KOI-784.01	541.9	25.6	4.9 σ	53.9	54.1	4.8 σ
KOI-784.02	29.0	7.2	3.3 σ	-	-	-
KOI-3284.01	176.9	84.8	5.3 σ	97.9	5.0	3.3 σ
KOI-663.02	133.1	4.2	2.5 σ	116.6	15.0	2.9 σ
KOI-663.01	11.1	2.0	2.9 σ	50.1	7.1	5.4 σ
KOI-1596.02	1050.0	22.1	2.7 σ	802.7	48.5	1.7 σ
KOI-1596.01	36.1	24.1	2.7 σ	-	-	-
KOI-494.01	116.1	13.1	2.6 σ	116.1	33.9	2.7 σ
KOI-252.01	128.4	3.3	3.4 σ	81.1	12.9	2.9 σ

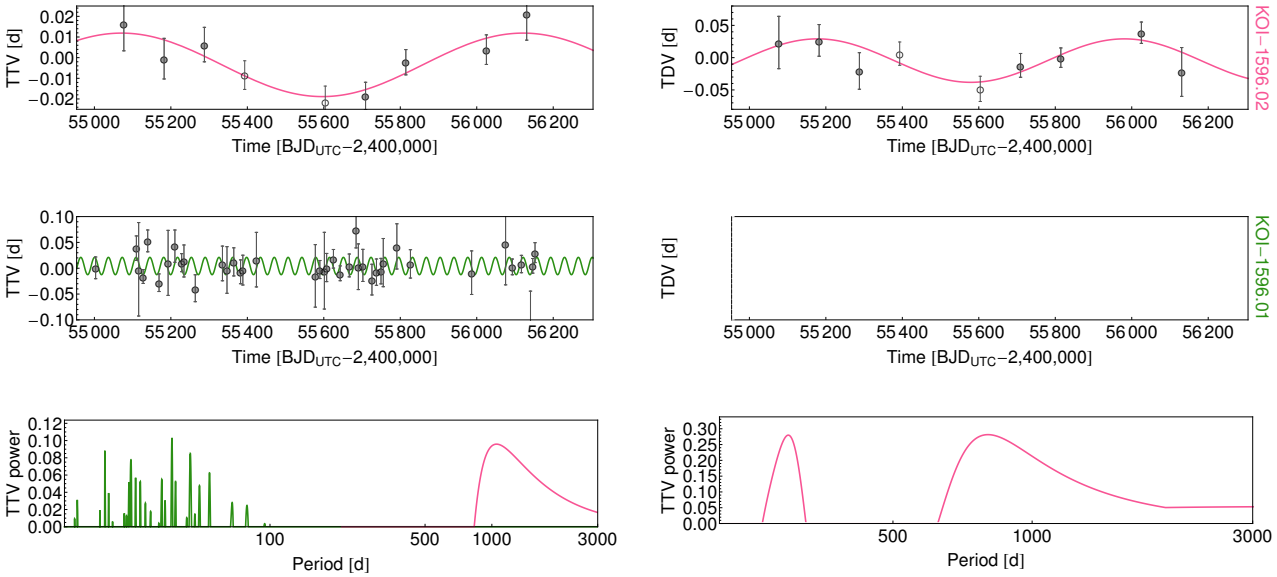

FIG. 4.— *TTVs (left) and TDVs (right) for the planetary candidates of KOI-1596. Each row shows the observations (circles) with the best-fit sinusoid from a periodogram using the same coloring as that for which the name of the planet is highlighted in on the RHS. For KOI-1596.02, points used in the photodynamical moon fits are filled circles, whereas those points ignored for subsequent predictive tests are open circles. Bottom panels show the periodograms of the TTVs & TDVs (which use the entire available data set), with vertical grid lines marking the locations where one might expect power from planet-planet interactions.*

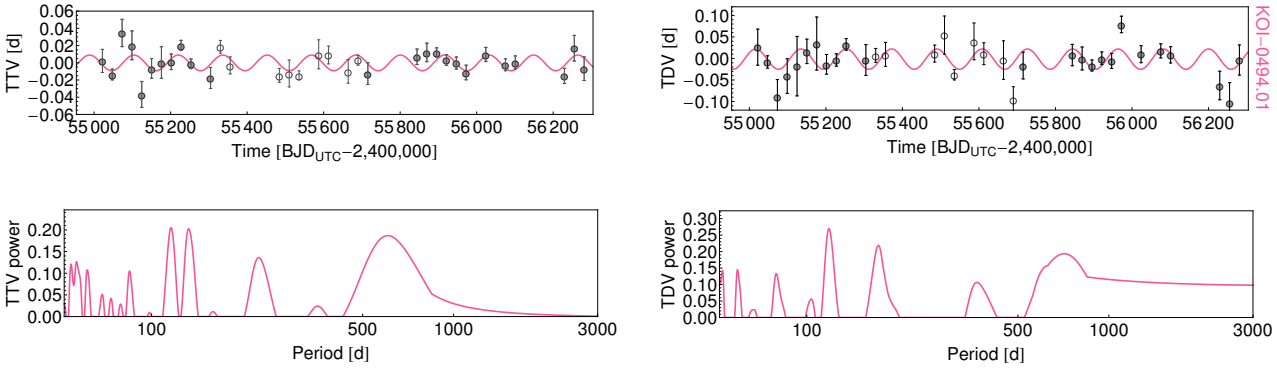

FIG. 5.— *TTVs (left) and TDVs (right) for the planetary candidate of KOI-494. Points used in the photodynamical moon fits are filled circles, whereas those points ignored for subsequent predictive tests are open circles. Bottom panels show the periodograms of the TTVs & TDVs (which use the entire available data set).*

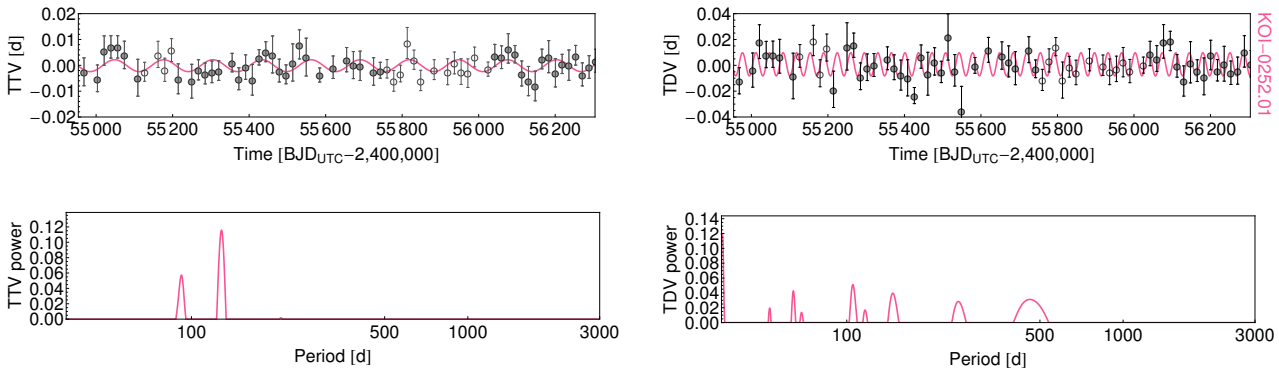

FIG. 6.— *TTVs (left) and TDVs (right) for the planetary candidate of KOI-252. Points used in the photodynamical moon fits are filled circles, whereas those points ignored for subsequent predictive tests are open circles. Bottom panels show the periodograms of the TTVs & TDVs (which use the entire available data set).*

KOI-314.02 and KOI-784.01 are the only two remaining KOIs and we classify these both as spurious dynamical detections. A-priori, these two systems have the highest chance of exhibiting significant planet-planet interactions since KOI-314.02 and KOI-314.01 reside near a 5:3 period commensurability and KOI-784.01 and KOI-784.02 are close to 2:1. In the case of KOI-314, there is a third planetary candidate interior to the other two, for which the closest commensurabilities are 9:4 and 5:4 relative to KOI-314.02 and KOI-314.01 respectively. Given that the 9:4 commensurabily does not usually exhibit strong perturbations and the fact KOI-314.03 is three times smaller than the other two KOIs, the lack of any observed interactions induced by this candidate is not surprising.

For both KOI-314.02 and KOI-784.01, the moon model $\mathcal{S}$ yields an (M_S/M_P) posterior peaking at unity (i.e. the solutions favor binary planets). Formally, all of the detection criteria are satisfied despite this, as seen in Table 4. From the TTVs shown in Figures 7 & 8 and the list of periodogram frequencies detailed in Table 5, it is clear that significant power exists at long-periods for both objects. Since exomoons always have an orbital period less than that of the planet they are bound to (Kipping 2009a), the moon interpretation requires these to be aliases of the true short period. However, producing such a long period requires fine tuning of the moon's period. This is easily visualized in Figure 9, where one can see that for both cases we require a moon's period to be nearly 1:2 commensurable to the planet's period, with a small frequency splitting which induces the longer super-period. Such fine tuning is a strong blow to the moon hypothesis since there is no known example of a Solar System moon being in such a near-commensurability.

A crude but useful tool in studying TTVs of multi-planet systems is to estimate the "super-period" of the TTVs assuming the variations are sinusoidal (Xie 2013). Consider two planets with orbital periods P' and P where $P' > P$. For two planets in a $k^{\rm th}$ order MMR, the ratio of the orbital periods is simply $(P'/P) \simeq j/(j-k)$, where k is an integer satisfying $0 < k < j$ and j defines the mutual proximity of the MMR. Following the approximate theory of Xie (2013), the expected periodicity of the observed TTVs, the so-called "super-period", is given by:

$$\Delta \equiv \left(\frac{P'}{P}\right)\left(\frac{j-k}{j}\right) - 1, \quad (3)$$

$$P_{\rm TTV} = \frac{P'}{j|\Delta|}. \quad (4)$$

For the KOI-314 and KOI-784 systems, we have marked $P_{\rm TTV}$ on the periodograms shown in Figures 7 & 8. The pair KOI-314.01/.02 indeed shows power at this frequency and performing a full dynamical fit of the TTVs (described in the Appendix) retrieves a quasi-sinusoidal signal conforming with this frequency. In contrast, our dynamical fits of KOI-784.01/.02 reveal a non-sinusoidal waveform, which explains why the expected super-period has no accompanying power in the periodogram.

In both systems, the TTVs fitted by our moon model $\mathcal{S}$ produce an essentially equally good fit to the data as a planet-planet interaction model. This is clearly evident by comparing the fits shown in Figures 7 & 8. However, the moon model requires an entirely new object to be introduced into the system to explain the observations, whereas the planet-planet models naturally explain the TTVs simply using the known transiting planets. This fact, combined with the previously discussed concerns with the moon hypothesis, leads us to conclude that both KOI-314 and KOI-784 are spurious dynamical detections i.e. a planet-planet perturbation is the most likely underlying reason via Occam's Razor.

For both KOI-314 and KOI-784, we conducted two sets of dynamical TTV fits where we turned on/off the mass of the planets. Since our fits are conducted with MULTINEST, we may compare the Bayesian evidences to evaluate the statistical significance of the claimed interactions, for which we find healthy confidences of $24.2\,\sigma$ and $6.7\,\sigma$ for KOI-314.01/.02 and KOI-784.01/.02 respectively. The maximum a-posteriori fit through the TTVs & TDVs (where available) reduces the χ^2 from $1440.1 \rightarrow 335.2$ with 218 observations for KOI-314.01/.02 and $487.7 \rightarrow 340.0$ with 166 observations for KOI-784.01/.02. A simple F-test based on these χ^2 changes finds confidences of $17.1\,\sigma$ and $7.1\,\sigma$ for KOI-314.01/.02 and KOI-784.01/.02 respectively, showing good consistency with the Bayesian evidence calculation.

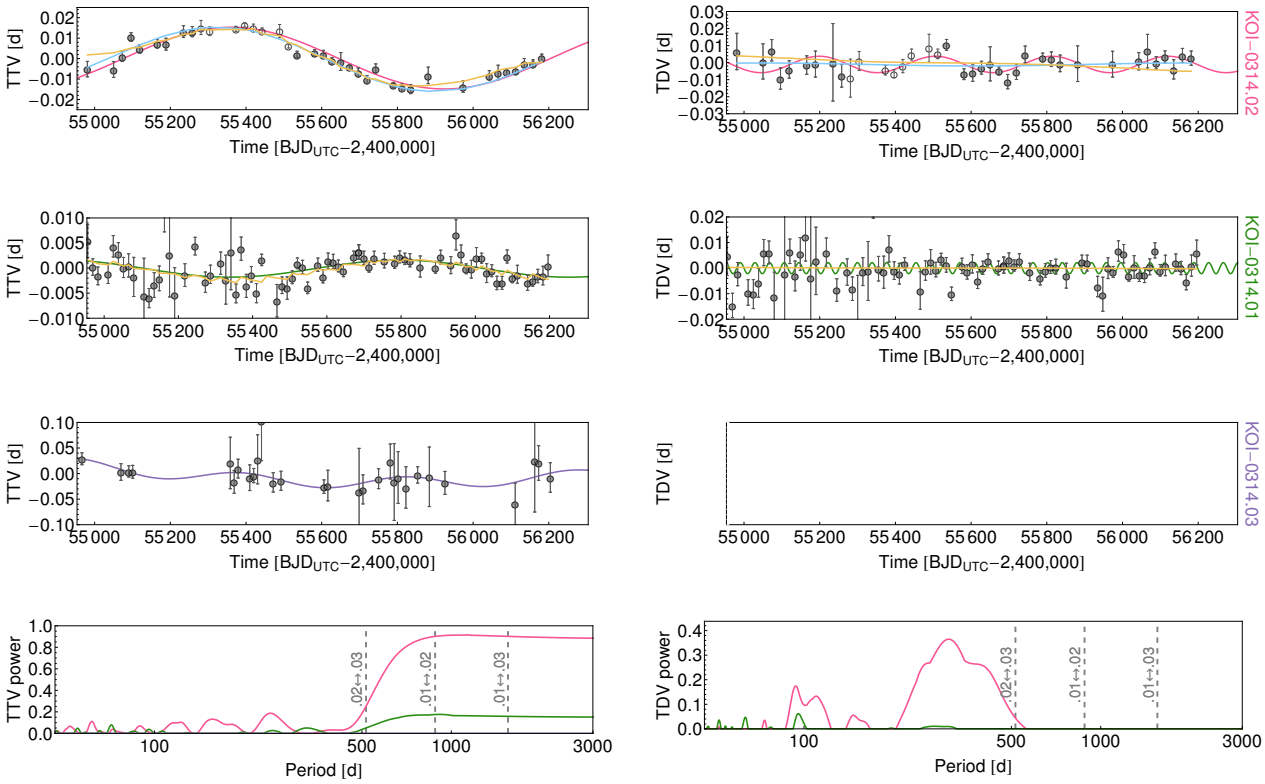

FIG. 7.— *TTVs (left) and TDVs (right) for the planetary candidates of KOI-314. Each row shows the observations (circles) with the best-fit sinusoid from a periodogram using the same coloring as that for which the name of the planet is highlighted in on the RHS. Additionally, we show the best-fit moon model in blue and best-fit planet-planet model in orange. For KOI-314.02, points used in the photodynamical moon fits are filled circles, whereas those points ignored for subsequent predictive tests are open circles. Bottom panels show the periodograms of the TTVs & TDVs (which use the entire available data set), with vertical grid lines marking the locations where one might expect power from planet-planet interactions.*

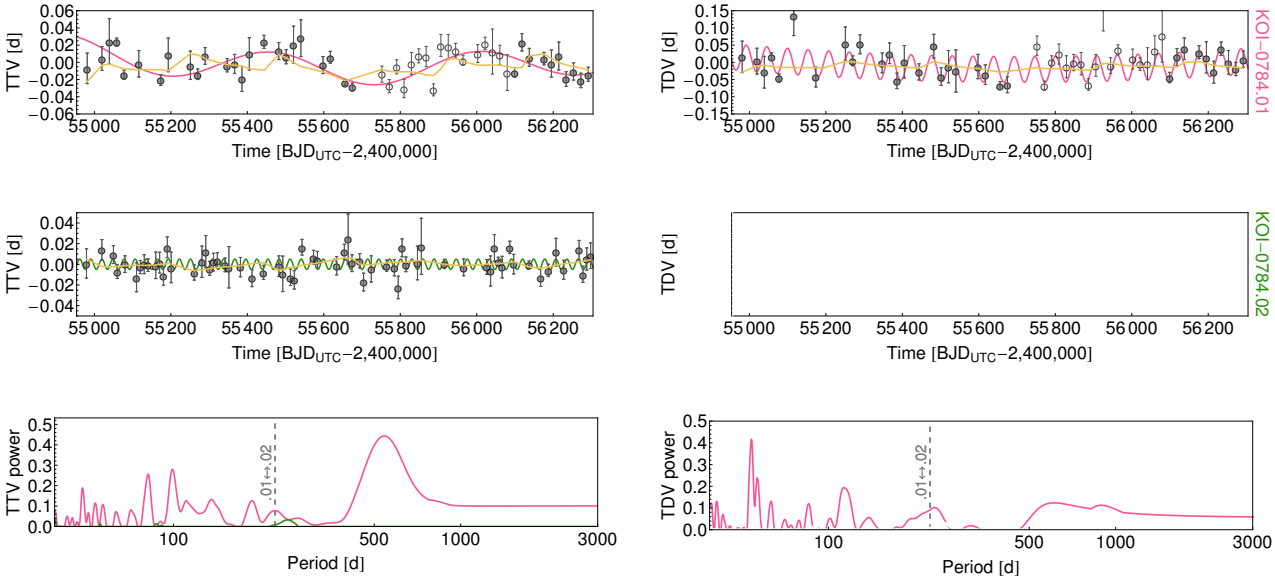

FIG. 8.— *TTVs (left) and TDVs (right) for the planetary candidates of KOI-784. Each row shows the observations (circles) with the best-fit sinusoid from a periodogram using the same coloring as that for which the name of the planet is highlighted in on the RHS. Additionally, we show the best-fit planet-planet model in orange. For KOI-784.01, points used in the photodynamical moon fits are filled circles, whereas those points ignored for subsequent predictive tests are open circles. Bottom panels show the periodograms of the TTVs & TDVs (which use the entire available data set), with vertical grid lines marking the locations where one might expect power from planet-planet interactions.*

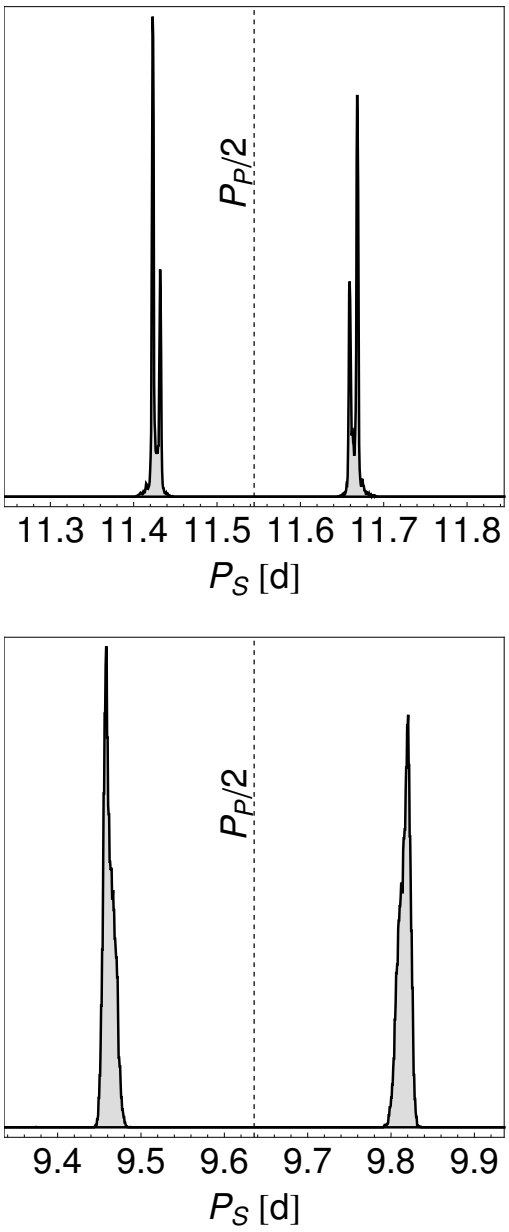

FIG. 9.— *Posterior distribution for a putative moon's orbital period for KOI-314.02 (upper panel) and KOI-784.01 (lower panel). In both cases, the observed long-period TTV requires a finely tuned moon period close to a 2:1 commensurability with the planet, which we deem quite improbable.*

Statistics aside, Figure 7 shows that our fits for KOI-314.01/02 clearly reproduce the dominant pattern in the data. The two sets of TTVs exhibit visible anti-correlation, which is a well-known signature of planet-planet interactions (Steffen et al. 2012) and so further improves our confidence in this fit. Finally, we note that the derived solution is dynamically stable for $\geq$ Gyr and yields physically plausible internal compositions for both objects (see Table 6).

Although MULTINEST only identifies one mode and thus the solution appears unique, the unweighted posteriors show high likelihood solutions extending down a thin tail of higher eccentricities and higher masses. These solutions have much lower sample probability since they require the fine tuning of $\Delta\varpi \simeq 0$ to explain the data. Given our assumption of uniform priors in ϖ, the likelihood multiplied by the prior mass, which defines the sample probability, is much lower along this tail and thus has a much lower Bayesian evidence. For this reason, this tail does not appear when MULTINEST outputs the weighted posteriors. We decided to explore this tail in a second fit by enforcing a lower limit of $(M_P/M_\star) > 1.5 \times 10^{-5}$. The mode which is picked up by MULTINEST down this tail is easily identified as unphysical, since it requires that 77.4% of KOI-314.01's posterior samples exceed the mass-stripping limit of Marcus et al. (2009) (i.e. the density is unphysically high). The fact the solution is both unphysical and has a much lower sample probability allows us to discard it.

We therefore consider the original solution to be the only plausible explanation for the TTVs. We subsequently consider these planetary candidates to be confirmed as exhibiting interactions and thus are real planets given the low derived masses. We refer to KOI-314.01 and .02 as KOI-314b and KOI-314c respectively from here on. Note that KOI-314.03 exhibits no detectable signature in any of the TTVs and thus this object remains a planetary candidate at this time.

Formally, our dynamical model for KOI-784.01/.02 is favored over a non-interacting model at $\sim 7\,\sigma$. Despite this, we prefer to consider these two objects a tentative detection at this time. Our caution is based on the fact that it is difficult to actually see any structure in the observed TTVs (see Figure 8). Further, there is an apparent lack of power in the .01 periodogram at the expected super-period and yet considerable power at ~ 500 d (see Table 5). Our best fitting TTV model does not reproduce any power at 500 d, but does have its dominant power at the super-period. For these reasons, it is unclear whether our model is just fitting out some non-white noise component remaining in the data. Despite this, we note that the derived solution is apparently unique, dynamically stable and again yields physically plausible internal compositions for both objects (see Figure 11). Our favored solution yields significant eccentricity for KOI-784.01 of $e = 0.182^{+0.014}_{-0.021}$, which is also noteworthy. We attempted to repeat the fits enforcing low eccentricities but this yielded an implausibly dense composition for KOI-784.01 with 99.1% of the trials exceeding the mass stripping limit of Marcus et al. (2009). We argue that confirmation of this signal could be made by collecting further TTVs or identifying an object responsible for the $\sim$500 d periodogram peak, either through transits or radial velocities.

Following the strategy of Nesvorný et al. (2012) for KOI-872b, we adjusted the time stamps of the detrended photometry for these two systems by offsetting the best-fitting dynamical planet-planet model transit times. Since the interacting planets must orbit the same star, this allows us to re-fit the photometry with a common mean stellar density ($\rho_\star$) and common limb darkening coefficients (q_1 and q_2) using a simple planet-only model. Combining this information yields improved and self-consistent parameters for each planet. In these fits, the eccentricity and argument of periastron passage for

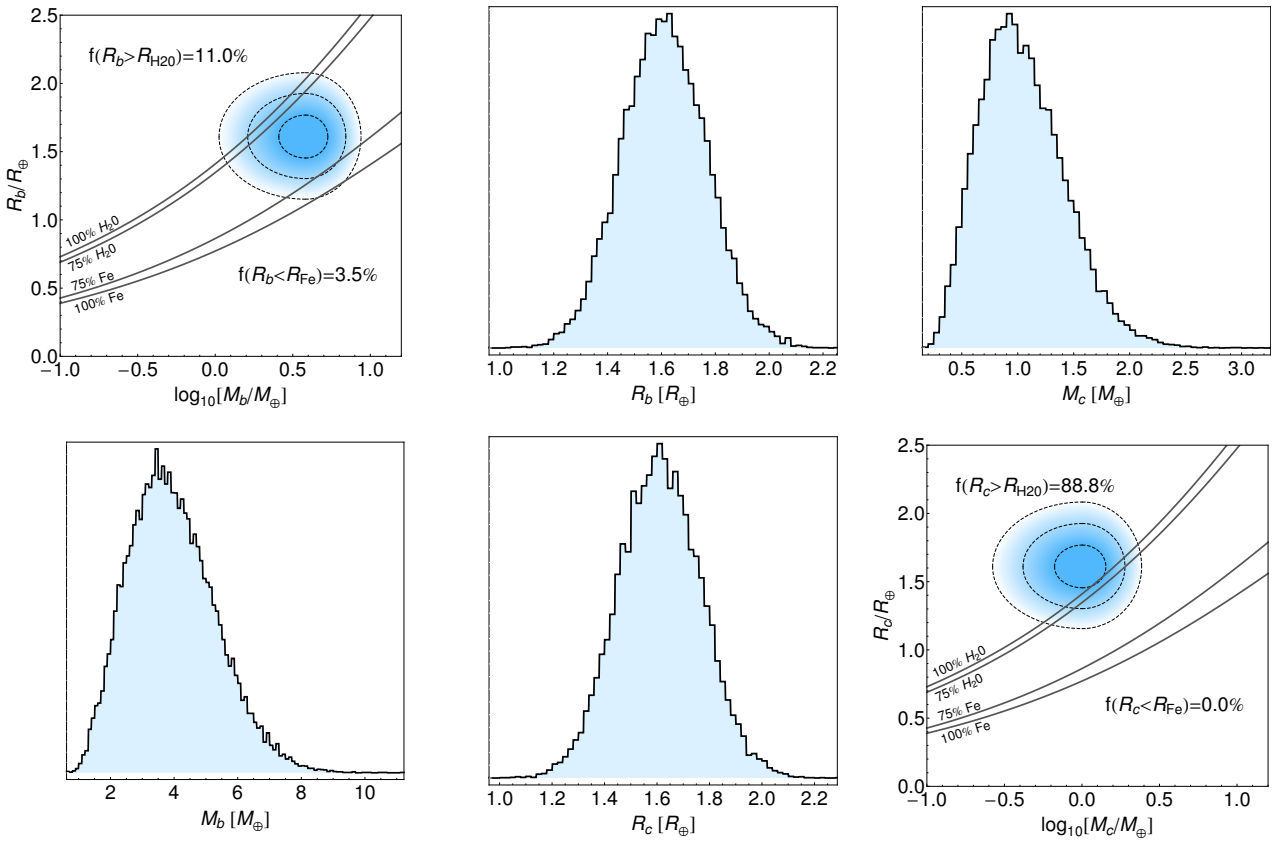

FIG. 10.— *Posterior distributions for the mass and radius of planets KOI-314b and KOI-314c. The joint posteriors in the corners reveal that the inner planet, b, is likely rocky, whereas the Earth-mass outer planet, c, likely maintains an extended atmosphere comprising* $\geq 17^{+12}_{-13}$ *% of the total radius.*

the planetary candidates are fixed to the maximum a-posteriori values from the dynamical fits (note they are all low eccentricity). This combined model is referred to as $\mathcal{C}_{bc}$, where the subscript denotes that planets b and c were assumed to orbit the same star. Rather than attempt to fit a moon model through these adjusted data, we take the conservative approach of simply stating that we cannot place any constraints on the presence of moons for these KOIs due to the strong planet-planet interactions.

Our derived final parameters for the KOI-314 and KOI-784 systems are provided in Table 6. It is worth noting that the light curve derived stellar density from KOI-314b and KOI-314c ($\rho_{\star,\rm obs}$) is $\sim 2\,\sigma$ discrepant with that expected from the stellar parameters derived by Pineda et al. (2013) ($\rho_{\star,\rm spec}$), with $(\rho_{\star,\rm obs}/\rho_{\star,\rm spec}) = 0.55^{+0.23}_{-0.16}$, whereas the other densities appear consistent. We suggest that this is likely a result of the adjusted photometry used to derive $\rho_{\star,\rm obs}$ containing some residual TTVs or TDVs due to either unaccounted for perturbing bodies or the unpropagated uncertainty of the best-fitting dynamical model itself. As discussed recently in Kipping (2013b), residual perturbations cause an underestimation of $\rho_{\star,\rm obs}$ via the photo-timing and photo-duration effects. Using the photo-timing expressions of Kipping (2013b), a residual TTV of $\simeq$2 minutes amplitude would be sufficient to explain the low $(\rho_{\star,\rm obs}/\rho_{\star,\rm spec})$ observation. This is entirely plausible given that the residuals of the best-fitting TTV model for KOI-314c exhibit an r.m.s. of 4.0 minutes. A light curve derived stellar density with improved accuracy and more realistic uncertainties could be derived using a full photodynamical model for the planet-planet interactions (Kipping 2013b), however this is outside the scope of this work and it is unclear what insights Asterodensity Profiling (AP) could provide superior to the TTVs in any case for this object.

4. DISCUSSION & CONCLUSIONS

4.1. *Discovery of an Earth-mass Planet*

Although it is not the principal goal of our work, a by-product of our dynamical investigations has yielded the confirmation of an Earth-mass planet, KOI-314c, and a super-Earth, KOI-314b. KOI-314c is the lowest mass transiting planet discovered to date (see Figure 12), with a mass of $M_P = 1.0^{+0.4}_{-0.3}\,M_\oplus$. This may be compared to the next lowest mass transiting object currently known, Kepler-78b (Sanchis-Ojeda et al. 2013), with $M_P = 1.7 \pm 0.4\,M_\oplus$ (Howard et al. 2013; Pepe et al. 2013) determined using the radial velocity method. Remarkably, whereas Kepler-78b has a density similar to that of the Earth and thus is likely rocky, KOI-314c is 60% larger than the Earth with a mean density around four times lower at $\rho_P = 1.3^{+0.8}_{-0.5}\,\mathrm{g\,cm^{-3}}$.

Insights into the composition of this Earth-mass, but decidedly non-Earth-like, world can be gleaned by computing the "minimum atmospheric height" ($R_{\rm MAH}$), as discussed in Kipping et al. (2013c). For KOI-314c, we

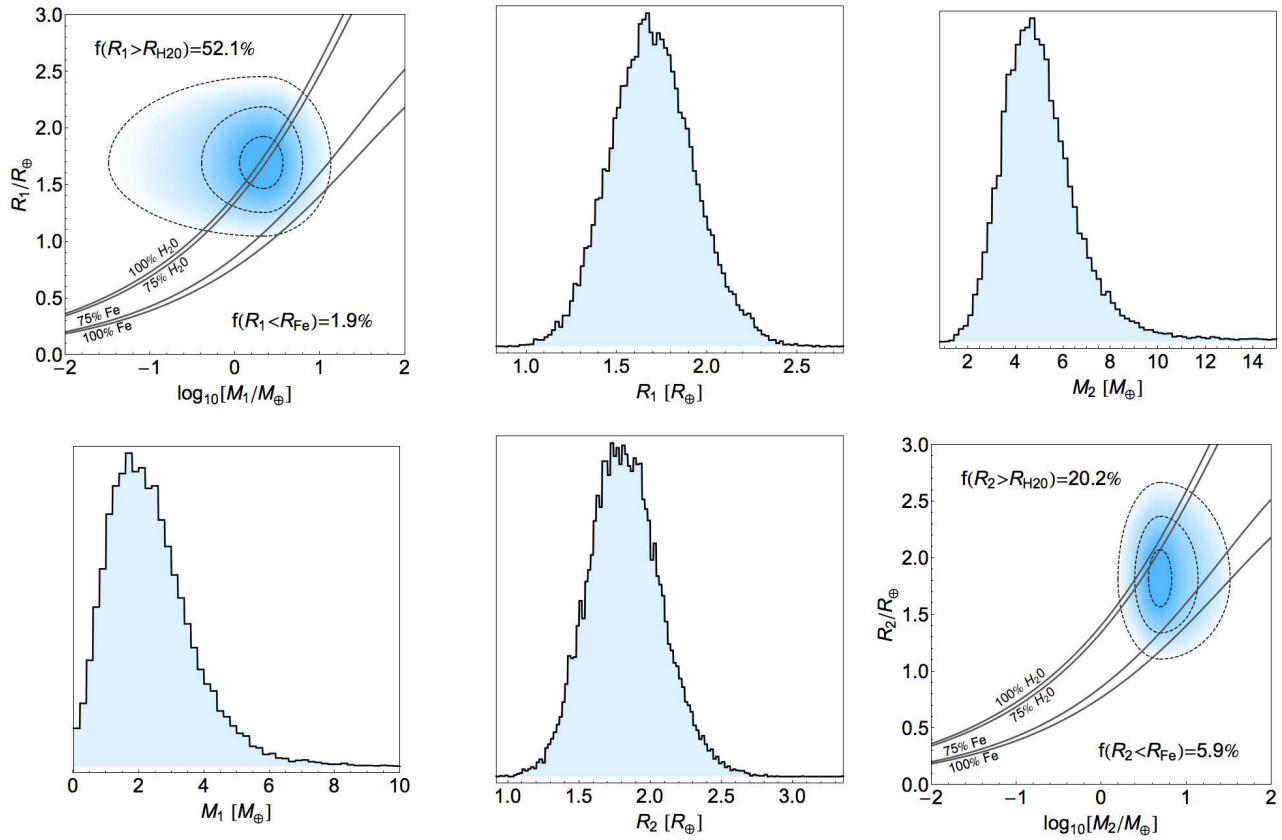

FIG. 11.— *Posterior distributions for the mass and radius of planetary candidates KOI-784.01 and KOI-784.02. The joint posteriors in the corners show physically sound compositions, where the outer body (.01) has a lower density than the inner world (.02).*

TABLE 6

*Final parameter estimates for the KOI-314 and KOI-784 systems. Parameters come from both a transit light curve model and a dynamical TTV model to account for the planet-planet perturbations between KOI-314b/c and KOI-784.01/.02. For these two pairs of objects, the transit model assumes a common star. Reference epochs of 770 & 800 BKJD$_{\rm UTC}$ are used for the dynamical fits of KOI-314 & KOI-784 respectively, where BKJD$_{\rm UTC}$ =BJD$_{\rm UTC}$ − 2,454,833. * = fixed quantity.*

KOI	314b	314c	314.03	784.01	784.02
P	$13.78164^{+0.00019}_{-0.00014}$	$23.08933^{+0.00071}_{-0.00071}$	$10.312921^{+0.000060}_{-0.000064}$	$19.2729^{+0.0019}_{-0.0012}$	$10.06543^{+0.00018}_{-0.00016}$
τ [BKJD$_{\rm UTC}$] ...	$742.87635^{+0.00033}_{-0.00040}$	$725.1404^{+0.0014}_{-0.0013}$	$741.9915^{+0.0021}_{-0.0022}$	$803.4428^{+0.0021}_{-0.0021}$	$800.5997^{+0.0021}_{-0.0020}$
$(M_P/M_\star) \times 10^{-5}$	$2.03^{+0.76}_{-0.65}$	$0.53^{+0.21}_{-0.18}$	-	$1.31^{+0.84}_{-0.63}$	$2.89^{+0.97}_{-0.71}$
$(R_P/R_\star)$	$0.02730^{+0.00087}_{-0.00070}$	$0.02731^{+0.00085}_{-0.00072}$	$0.00753^{+0.00078}_{-0.00050}$	$0.0322^{+0.0020}_{-0.0015}$	$0.0345^{+0.0025}_{-0.0019}$
e	$0.050^{+0.049}_{-0.025}$	$0.024^{+0.030}_{-0.016}$	-	$0.182^{+0.014}_{-0.021}$	$0.027^{+0.027}_{-0.018}$
ω [°]	72^{+47}_{-28}	170^{+130}_{-120}	-	$18.4^{+8.0}_{-5.7}$	170^{+130}_{-110}
Ω [°]	270*	300^{+40}_{-150}	-	270*	0^{+140}_{-140}
$\rho_{\star,\rm obs}$ [g cm^{-3}] ...	$2.75^{+0.70}_{-0.47}$	$2.75^{+0.70}_{-0.47}$	$5.3^{+2.1}_{-1.9}$	$5.2^{+1.4}_{-1.8}$	$5.2^{+1.4}_{-1.8}$
b	$0.922^{+0.011}_{-0.015}$	$0.767^{+0.033}_{-0.048}$	$0.31^{+0.28}_{-0.21}$	$0.32^{+0.27}_{-0.22}$	$0.838^{+0.046}_{-0.033}$
q_1	$0.355^{+0.074}_{-0.051}$	$0.355^{+0.074}_{-0.051}$	$0.79^{+0.15}_{-0.24}$	$0.65^{+0.22}_{-0.24}$	$0.65^{+0.22}_{-0.24}$
q_2	$0.45^{+0.32}_{-0.28}$	$0.45^{+0.32}_{-0.28}$	$0.84^{+0.12}_{-0.24}$	$0.58^{+0.25}_{-0.28}$	$0.58^{+0.25}_{-0.28}$
M_P [$R_\oplus$]	$3.83^{+1.51}_{-1.26}$	$1.01^{+0.42}_{-0.34}$	-	$2.2^{+1.5}_{-1.1}$	$4.9^{+1.8}_{-1.3}$
R_P [$R_\oplus$]	$1.61^{+0.16}_{-0.15}$	$1.61^{+0.16}_{-0.15}$	$0.446^{+0.062}_{-0.050}$	$1.69^{+0.24}_{-0.23}$	$1.82^{+0.26}_{-0.25}$
ρ_P [g cm^{-3}]	$5.0^{+3.0}_{-2.0}$	$1.31^{+0.82}_{-0.54}$	-	$2.5^{+2.6}_{-1.4}$	$4.6^{+3.7}_{-1.9}$
$R_{\rm MAH}/R_P$	$-0.20^{+0.16}_{-0.18}$	$0.17^{+0.12}_{-0.13}$	-	$0.01^{+0.21}_{-0.23}$	$-0.27^{+0.32}_{-0.33}$
u_1	$0.80^{+0.19}_{-0.27}$	$0.80^{+0.19}_{-0.27}$	$1.57^{+0.22}_{-0.35}$	$1.17^{+0.26}_{-0.35}$	$1.17^{+0.26}_{-0.35}$
u_2	$-0.20^{+0.32}_{-0.22}$	$-0.20^{+0.32}_{-0.22}$	$-0.70^{+0.27}_{-0.15}$	$-0.40^{+0.31}_{-0.21}$	$-0.40^{+0.31}_{-0.21}$
$S_{\rm eff}$ [$S_\oplus$]	$6.8^{+1.5}_{-1.3}$	$3.39^{+0.74}_{-0.65}$	$9.9^{+2.1}_{-1.9}$	$3.34^{+1.05}_{-0.86}$	$7.8^{+2.5}_{-2.0}$

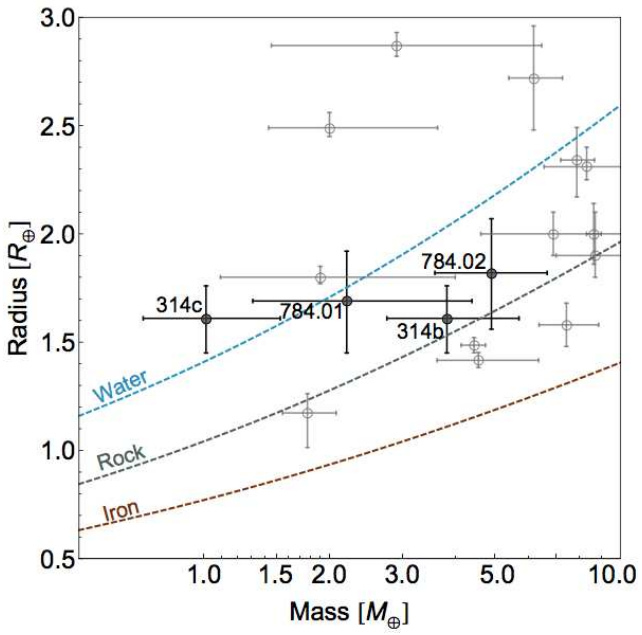

FIG. 12.— *Masses and radii of all confirmed transiting planets at the time of writing (gray points). The parameters for KOI-314b/c and KOI-784.01/.02 derived in this work are shown black, which includes the lowest mass transiting planet to date, KOI-314c. The dashed lines represent internal composition models from Zeng & Sasselov (2013) assuming no atmosphere.*

estimate $R_{\rm MAH} = 0.27^{+0.22}_{-0.22}\,R_\oplus$, which would constitute 17^{+12}_{-13}% of the planet by radius fraction. The confidence of an atmosphere being present is 89.3% using the technique described in Kipping et al. (2013c). It therefore seems probable that KOI-314c is enveloped in a gaseous light atmosphere, for which a H/He composition would be the most plausible candidate.

With a low density and thus low surface gravity of just $g = 3.8^{+2.0}_{-1.5}\,{\rm m\,s^{-2}}$, KOI-314c should have a considerable scale height. Using Equation 36 of Winn (2010), we estimate that the amplitude of the transmission spectroscopy signal may be up to 60 ppm, which may be compared to the transit depth of 620 ppm i.e. ∼10%. In addition, whilst KOI-314 has a magnitude of 12.9 in *Kepler's* bandpass, the target becomes quite bright towards the infrared with $K = 9.5$ (Cutri et al. 2003). Thus, KOI-314c is not only the first Earth-mass transiting planet but also the first potentially characterizable Earth-mass planet. Radial velocity measurements are unlikely to directly improve the mass estimate since we expect a semi-amplitude of $0.33^{+0.13}_{-0.11}\,{\rm m/s}$ due to planet c. However, we do predict a potentially detectable $1.50^{+0.56}_{-0.48}\,{\rm m/s}$ due to planet b, whose determination may aid in refining our dynamical solution.

Both the KOI-314b/c pair and the KOI-784.01/.02 pair appear to have properties consistent with a history of photo-evaporation. In both cases, we have one inner planet with a density consistent with a mostly rocky world and one outer planet with a density suggestive of a significant gaseous envelope (although KOI-784.02 can also be explained as being a nearly pure water world). This dichotomy has been seen previously with Kepler-36b/c (Carter et al. 2012), which Lopez & Fortney (2013a) attributed as a signature of photo-evaporation. The incident bolometric fluxes for KOI-314b/c and KOI-784.01/.02 are modest at $\lesssim 10\,S_\oplus$ (see Table 6) and thus less than the typical level expected to induce photo-evaporation (Lopez & Fortney 2013b). However, the EUV and X-ray fluxes may be significantly enhanced for M-dwarf stars, such as KOI-314 and KOI-784, meaning it is quite plausible that photo-evaporation may be responsible for the observed densities.

4.2. *Exomoon Survey Results*

In this survey, we find no compelling evidence for an exomoon around any of the eight KOIs analyzed. Out of these eight, we find five null detections and one spurious photometric detection and we are able to derive robust upper limits on the satellite-to-planet ratio, (M_S/M_P), in these cases. The other two KOIs are spurious dynamical detections for which we are unable to derive any upper limits on (M_S/M_P). The final posterior distributions for (M_S/M_P) are shown in Figure 13.

Our fits only provide limits on (M_S/M_P) and not M_S directly. Since the planetary masses of the six constrained cases are unknown, then M_S cannot be observationally constrained. If we assume the planetary candidates are real, then one may invoke a mass-radius relation to provide an approximate estimate of the typical M_S values being probed in our survey. For this calculation, we use the empirical two-component mass-radius relation recently derived by Weiss & Marcy (2013) from 63 KOIs with radii below 4 Earth radii (appropriate for our sample). This yields $M_S \lesssim 4.4, 0.36, 1.3, 3.2, 3.3$ & 2.2 $M_\oplus$ to 95% confidence for KOI-463.01, 3284.01, 663.02, 1596.02, 494.01 & 252.01 respectively. This may be compared to the seven objects studied in survey I (Kipping et al. 2013a), for which we find $M_S \lesssim 0.09, 4.2, 5.9, 0.36, 0.17, 1.32$ & $0.07\,M_\oplus$ for KOI-722.01, 365.01, 174.01, 1472.01, 1857.01, 303.01 & 1876.01 respectively. In general, survey I certainly probed down to lower (M_S/M_P) ratios but the actual limits on M_S are only modestly better for the survey I sample than this survey.

Although survey I appears to probe down to lower limits, it is unclear exactly why this is the case. Although survey I defined no precise constraints on the stellar hosts, almost all of the stars are K/G-dwarfs with a median effective temperature of 5600 K versus 3800 K for the sample studied here. From the basics of exomoon detection theory, one should expect the dominant constraint to come from the TTV effect which scales as $\sim (M_S/M_P) a_{SB} P_P / a_{B*}$ (Sartoretti & Schneider 1999; Kipping 2011b). Replacing a_{SB} and a_{B*} with period-related terms via Kepler's Third Law, we therefore expected $(M_S/M_P) \sim {\rm TTV}/(pP_P)$. We find no empirical correlation between our derived (M_S/M_P) limits and this term using several reasonable metrics to quantify the TTV signal-to-noise. Similarly, variants of the signal-to-noise of the transits appear to have no clear correlation to the derived (M_S/M_P) limits either. This may be because our sample is still relatively small and thus it remains difficult to identify anomalous points which skew the sample.

With this paper, the HEK project has now surveyed 17 planetary candidates for evidence of an exomoon (Nesvorný et al. 2012; Kipping et al. 2013a,b and this

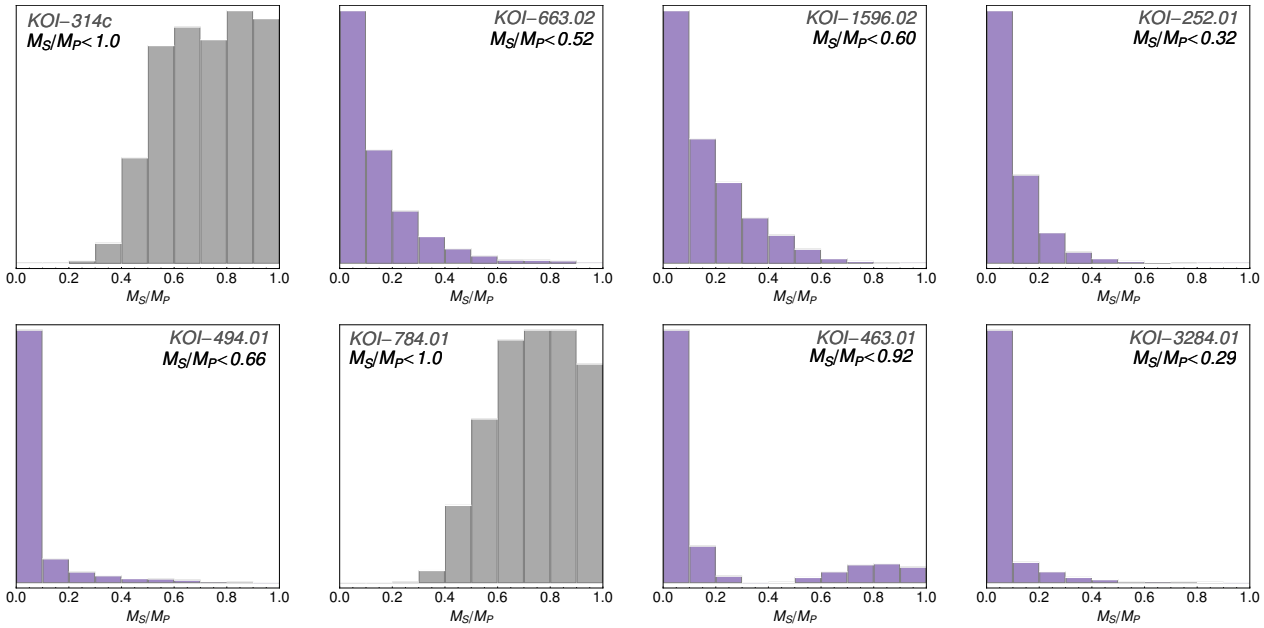

FIG. 13.— *Posterior distributions for the mass ratio between a putative exomoon and the Kepler planetary candidates studied in this work. KOI-314c and KOI-784.01 are dynamical spurious detections induced by planet-planet interactions. KOI-252.01 is a photometric spurious detection and so we provide the posterior from model $\mathcal{S}_{R0}$ to provide a corrected estimate of the mass-ratio upper limit. The remaining five planetary candidates are null-detections.*

work). In all cases, we find no compelling evidence for such an object with considerable range in the derived upper limits on the satellite-to-planet mass ratio down to 1% and upper limits on the (estimated) satellite mass down to $0.1\,M_\oplus$. As discussed in the last paragraph, it remains unclear why such diversity exists in our carefully selected sample. However, the best case sensitivities match the predictions made in Kipping et al. (2009), supporting the hypothesis that *Kepler* is capable of detecting sub-Earth mass moons. At this stage, with just 17 objects surveyed, the sample size is too small to deduce any meaningful occurrence rate statistics although it would seem that large moons are at least not ubiquitous. In future work, we will expand the sample with the ultimate goal of providing a measurement of the occurence of large moons around viable planet hosts, $\eta_{\leftmoon}$.

ACKNOWLEDGEMENTS

We would like to thank René Heller for his thoughtful review which improved the quality of our manuscript. This work made use of the Michael Dodds Computing Facility. DMK is funded by the NASA Carl Sagan Fellowships. JH and GB acknowledge partial support from NSF grant AST-1108686 and NASA grant NNX12AH91H. DN acknowledges support from NSF AST-1008890. We offer our thanks and praise to the extraordinary scientists, engineers and individuals who have made the *Kepler Mission* possible. Without their continued efforts and contribution, our project would not be possible.

REFERENCES

Barnes, J. W. & O'Brien, D. P., 2002, ApJ, 575, 1087
Bennett, D. P. et al., 2013, arXiv:1312.3951
Bonfils, X. et al., 2013, A&A, 549, 109
Carter, J. A. et al., 2012, Science, 337, 556
Christiansen, J. L. et al., 2012, PASP, 124, 1279
Cutri, R. M. et al., 2003, VizieR Online Data Catalog, 2246, 0
Domingos, R. C., Winter, O. C. & Yokoyama, T., 2006, MNRAS, 373, 1227
Dong, S. & Zhu, Z., 2013, ApJ, 778, 53
Dressing, C. D. & Charbonneau, D., 2013, ApJ, 2013, 767, 95
Feroz, F. & Hobson, M. P., 2008, MNRAS, 384, 449
Feroz, F., Hobson, M. P. & Bridges, M., 2009, MNRAS, 398, 1601
Forgan, D. & Kipping, D. M., 2013, MNRAS, 432, 2994
Fressin, F. et al., 2013, ApJ, 677, 81
Heller, R., 2012, A&A, 545, 8
Heller, R. & Barnes, R., 2013, AsBio, 13, 18
Howard, A. W. et al., Science, 330, 653
Howard, A. W. et al., 2013, Nature, 503, 381
Kipping, D. M., Fossey, S. J., Campanella, G., 2009, MNRAS, 400, 398
Kipping, D. M., 2009a, MNRAS, 392, 181
Kipping, D. M., 2009b, MNRAS, 396, 1797
Kipping, D. M., 2010, MNRAS, 408, 1758
Kipping, D. M. & Tinetti, G., 2010, MNRAS, 407, 2589
Kipping, D. M., 2011a, MNRAS, 416, 689
Kipping, D. M., 2011b, PhD thesis, University College London (astro-ph:1105.3189)
Kipping, D. M., Bakos, G. Á., Buchhave, L. A., Nesvorný, D. & Schmitt, A. 2012, ApJ, 750, 115
Kipping, D. M., 2013a, MNRAS, 435, 2152
Kipping, D. M., 2013b, MNRAS, submitted (arXiv:1311.1170)
Kipping, D. M., Hartman, J., Buchhave, L. A., Schmitt, A., Nesvorný, D. & Bakos, G. Á., 2013a, ApJ, 770, 101
Kipping, D. M., Forgan, D., Hartman, J., Nesvorný, D., Bakos, G. Á., Schmitt, A. R. & Buchhave, L. A., 2013b, ApJ, 777, 134
Kipping, D. M., Spiegel, D. S. & Sasselov, D., 2013, MNRAS, 434, 1883
Levison, H. F. & Duncan, M. J., 1994, Icarus, 108, 18
Lopez, E. D. & Fortney, J. J., 2013a, ApJ, 776, 2
Lopez, E. D. & Fortney, J. J., 2013b, ApJ, submitted (arXiv:1311:0329)
Lucy, L. B. & Sweeney, M. A. 1971, AJ, 76, 544
Mandel, K. & Agol, E., 2002, ApJ, 580, 171

Mann, A. W., Gaidos, E. & Ansdell, M., 2013, ApJ, 779, 188
Marcus, R. A., Stewart, S. T., Sasselov, D. & Hernquist, L., 2009, ApJ, 700, 118
Mayor, M. et al., 2011, arXiv:1109.2497
Muirhead, P. S., Hamren, K., Schlawin, E., Rojas-Ayala, B., Covey, K. R., Lloyd, J. P., 2012, ApJ, 750, 37
Muirhead, P. S. et al., 2014, ApJ, submitted
Nevsorný, D., Kipping, D. M., Buchhave, L. A., Bakos, G. Á., Hartman, J. & Schmitt, A. R., 2012, Science, 336, 1133
Nevsorný, D., Kipping, D. M., Terrell, D., Hartman, J., Bakos, G. Á. & Buchhave, L. A., 2013, ApJ, 777, 3
Pepe, F. et al., 2013, Nature, 503, 377
Petigura, E. A., Howard, A. W. & Marcy, G. W., arXiv:1311.6806
Pineda, S. J., Bottom, M. & Johnson, J. A., 2013, ApJ, 767, 28
Sanchis-Ojeda, R., Rappaport, S., Winn, J. N., Levine, A., Kotson, M. C., Latham, D. W., Buchhave, L. A., 2013, ApJ, 774, 54
Sartoretti, P. & Schneider, J., 1999, A&AS, 14, 550
Steffen, J. H. et al., 2012, MNRAS, 421, 2342
Weiss, L. M. & Marcy, G. W. 2013, ApJL, submitted (arXiv:1312.0936)
Williams, D. M., Kasting, J. F. & Wade, R. A., 1997, Nature, 385, 234
Winn, J. N., 2010, *Transits and Occultations*, EXOPLANETS, University of Arizona Press; ed: S. Seager
Wisdom, J. & Holman, M., 1991, AJ, 102, 1528
Wisdom, J., Holman, M. & Touma, J., 2006, FIC, 10, 217
Xie, J.-W., 2013, ApJS, 208, 22
Zeng, L. & Sasselov, D., 2013, PASP, 125, 227

APPENDIX:PLANET-PLANET DYNAMICAL FITS

We here provide details on how the dynamical planet-planet fits to the TTVs and TDVs were executed. In all cases, the regressions were executed using MultiNest (Feroz et al. 2008, 2009), which is able to fully explore complex and multi-modal parameter space and report on the uniqueness and relative significances of any modes identified. The dynamical model called by MultiNest considers the planets placed in general orbits, which are numerically integrated forward in time using a code based on a symplectic N-body integrator known as `swift_mvs` (Levison & Duncan 1994). `swift_mvs` is an efficient implementation of the second-order map developed by Wisdom & Holman (1991) and in practice we apply a symplectic corrector to improve the integrator's accuracy, as discussed in Wisdom et al. (1996).

Our model computes the mid-transit times and durations by interpolation as described in Nesvorný et al. (2013). With an integration time step of 1/20 of the orbital period, the typical precision is better than a few seconds, which is better than needed because the measurements generally have >1 minute errors. We use MultiNest with a Gaussian likelihood function on the transit times and durations, using 4000 live points and a target efficiency of 0.1, to fully explore the parameter space and locate plausible solutions.

The low radius of KOI-314.03 coupled with the lack of period commensurability meant that TTVs from this object would be $\lesssim$seconds in amplitude and thus would be undetectable with our measurements. For both KOI-314 and KOI-784 then, we only consider dynamical two-planet fits. Accordingly, the dynamical model has 14 parameters: the mass ratios $(M_1/M_\star)$ & $(M_2/M_\star)$, the orbital periods P_1 & P_2, the time for each planet to evolve on an unperturbed orbit from $t_{\rm ref}$ to the mid-transit time of a selected transit (τ_1 & τ_2; see Carter et al. 2012), eccentricities e_1 & e_2, pericenter longitudes ϖ_1 & ϖ_2, nodal longitude difference $\Delta\Omega = (\Omega_2 - \Omega_1)$, impact parameters b_1 & b_2, and stellar density $\rho_\star$.

We use the transit reference system (Nesvorný et al. 2012), where the nodal longitude $\Omega_1 = 270^\circ$ by definition, and we define the reference inclination, ι, to be zero when the impact parameter, b, is zero. The reference time, $t_{\rm ref}$, was chosen to be close to the mid-transit time of a selected transit. Uniform priors were used for all parameters, except for $\rho_\star$, for which we used a Gaussian prior based on the spectoscopic stellar parameters (and held M_* fixed at the best-fit value). Note that the parameters P_1 & P_2 are the *osculating* periods at $t_{\rm ref}$ and as such they are not exactly equal to the *mean* periods inferred from the photometric analysis.